Supporting Information

Choi and Mitchison 10.1073/pnas.1221312110

SI Results and Discussion

Specificity of Granzyme B Cleavage Sequence. Although we did not perform exhaustive experiments measuring the susceptibility of the Granzyme B (GzmB) reporter to each specific caspase, the presented data suggests that the cleavage sequence, VGPDFGR in the GzmB reporter, is unlikely to be activated by other caspases. Fig. 1 *B–D* shows that treatment of HeLa cells with 2 μM staurosporine for 4 h does not activate the GzmB reporter. Similar concentrations of staurosporine have been shown to activate the following caspases in HeLa cells in 4 h or less: caspase-2 (figure 4 of ref. 1), caspase-3 (figure 1 of ref. 2), caspase-8 (figure 8 of ref. 3), and caspase-9 (figure 1 of ref. 2). Similarly, Fig. S2 *D–F* shows that treatment of MCF7 cells with 2 μM staurosporine for 6 h does not activate the GzmB reporter. Treatment of MCF7 cells with 1.5 μM staurosporine has been shown to activate caspsae-2, caspase-6, caspase-7, caspase-8, and caspase-9 within 4 h (figure S5 of ref. 4). In addition, Fig. S2 *G–J* shows that treatment of HeLa cells with 10 ng/mL TNFα and 10 μM cycloheximide for 6 h does not activate the GzmB reporter. Treatment of HeLa cells with the same dose of TNFα and cycloheximide has been shown to induce caspase-1 and caspase-4 within 5 h (figure 5 of ref. 5). Thus, interpreting our control experiments with published data suggests that caspase-1, -2, -3, -4, -6, -7, -8, and -9 are unlikely to cleave the GzmB reporter.

Thornberry et al. have also defined the tetrapeptide substrate cleavage specificities of the caspases (figure 1 of ref. 6). Although tetrapeptide specificities do not necessarily translate into full protein specificities, they suggest that the sequence VGPD is unlikely to be cleaved by standard caspases. A valine residue at the P4 position is not recognized by caspase-1, 2, -3, or -7, and with minimal activity for caspase-4 and -5. A glycine residue at the P3 position is not recognized by caspase-4, -5, -6, -8, or -9, and with minimal activity by caspase-2 and -3. A proline residue at the P2 position is not recognized by caspase-6 and -9, and with minimal activity by caspase-1 and -4. These results suggest that cleavage of VGPD may be inefficient by all of the major caspases.

Sequential and Not Simultaneous Killing. At the 3-min time resolution of time lapses, and using the GzmB reporter, it may appear that subsequent targets are killed simultaneously. However, higher time resolution imaging of calcium transients in target cells (Movie S4) shows that lethal hits are delivered sequentially, not simultaneously, to targets.

Another possibility is that the granzyme/perforin package from the first lethal hit leaks over into adjacent targets. In this case, the subsequent hits could be considered a direct consequence of the first hit and, hence, still simultaneous killing events rather than true sequential hits. However, killing via leakage from the first hit is unlikely to occur. The volume of an immunological synapse is estimated to be less than 5 μm^3 (7). If the average target radius is 20 μm, on average, the distance to the nearest adjacent target's membrane from the immunological synapse will be on the order of 10 μm. Then, the contents of the immunological synapse will be diluted by ∼1,000-fold (volume of sphere with radius 10 μm divided by 5 μm^3). If the average GzmB load is reduced by 1,000-fold, the GzmB reporter signal in the adjacent target would take about ∼1,000-fold longer to become visible, but such slow kinetics are not the case and the GzmB signal appears within a similar time frame for all targets.

Thus, similar amounts of GzmB are delivered to each target, which suggests that distinct synapses are delivering each lethal hit and, in turn, suggests that killing events are sequential and not simultaneous.

Zero Time Point of the Experiment. At the beginning of an experiment, effector cells are added to adherent targets in the well of a 96-well plate. The plate is then placed in an incubated microscope for imaging. The settling time of the effector cells is <10 min (Fig. S8*C*). A typical experiment would involve time lapse of 40 prerecorded positions. These positions and their focal planes were set after adding natural killer (NK) cells, which typically took more than 10 min to complete the procedure. Thus, NK cells were settled at the beginning of the imaging (Fig. S8 *A* and *B*).

The time necessary for the temperature and pH of the sample to equilibrate is unknown, but likely less than 30 min. For these reasons, it is not possible to define a clear $t = 0$, and the first kill time, t_1, of a single sample is poorly defined. However, a comparison between two different values of t_1 for two different samples within the same experimental trial is possible, because the equilibration time of the two samples is likely to be nearly identical.

For effector cells that already had at least one kill by the first imaging time point, a first kill value of $t_1 = 0$ was assigned. This occurred occasionally for HeLa targets, but almost never for MCF7 targets. Thus, the difference between the average first kill times of the two target lines is even larger than reported, further supporting the conclusions of the main text.

Time Constraints of Imaging. Killing activity of individual effector cells can be imaged for periods longer than 6 h. However, the interpretation of complex dynamics from longer movies is ambiguous. For the analysis of time lapses less than 6 h, killing dynamics due purely to cell signaling can be distinguished from dynamics due to gene expression by using cycloheximide or other expression inhibitors. However, cell health of both effector and target cells is likely perturbed in the presence of cycloheximide for long times beyond 6 h. It is then difficult to separate slow, expression-driven changes of cell state from the types of kinetic mechanisms discussed in the main text. Other factors, such as the cell cycle, may also contribute to dynamics on a very long time scale. For these reasons, the interpretation and analysis of the dynamics is most detailed for time lapses that are not too long.

Further Analysis of Single-Cell Dynamics. The conclusion that first killing times and subsequent waiting times have distinct rates and regulation are already supported by the arguments in the main text. However, for completeness, we include additional quantitative analysis of the single-cell dynamics that leads to conclusions consistent with the main text.

Although we stated previously that the zero time point of the experiment is undefined, we can apply a further analysis if we make the assumption that $t = 0$ of imaging is a valid zero time point. To support this assumption, we plotted the total number of kills for 6-min windows (Fig. S9*A*). Over the first hour of imaging, killing of HeLa targets shows a steady level of killing. The steady level suggests that the experimental model is already at equilibrium, in terms of effectors settling, pH, temperature, or other extrinsic factors.

We then take $t = 0$ as the absolute zero point and determine the waiting time distribution for any kill, starting at $t = 0$. For a memoryless process, the waiting time distribution will not depend on the reference point, whether that reference point is the previous kill or an arbitrary fixed point in time, such as our choice of $t = 0$. (In the main text, we concluded that the system may have

short-term memory, but here, we are starting the analysis again from simpler assumptions.) Then, the t_1 values from the main text can be considered as waiting times and directly compared with Δt from the main text after several adjustments.

We construct $p(\Delta T_1)$, where ΔT_1 corresponds to the waiting time for effectors making their first kill (Fig. S9 *B* and *C*). In contrast to $p(t_1)$ from Fig. 2, we do not include first kills occurring before $t = 0$, which is a substantial fraction of first kills for HeLa targets (~40%; Fig. 2*F*). For $p(\Delta T_1)$, we also make the adjustment of setting $t = 3$ min (the second frame) as the new zero point. The reason is that if we observe a kill exactly at $t = 0$, we cannot be sure if the first kill occurred at $t = 0$ or before. If we observe the first kill at $t = 3$ min, we can check the $t = 0$ frame to be sure that there was no kill then. In practice, this adjustment makes it possible to measure the correct value for $p(\Delta T_1 = 0)$. Although $p(\Delta T_1)_{\mathrm{HeLa}}$ is somewhat fit by a double exponential function corresponding to two sequential rate-limiting steps, $p(\Delta T_1)_{\mathrm{MCF7}}$ is clearly not (Fig. S9*D*). If the first bin is excluded, $p(\Delta T_1)_{\mathrm{HeLa}}$ is somewhat fit by an exponential decay, but $p(\Delta T_1)_{\mathrm{MCF7}}$ remains poorly fit (Fig. S9*D*). The poor fit suggests that the first kill for MCF7 has unique kinetics not explained by a simple rate constant, whereas the first kill for HeLa may be approximated by a rate constant.

We also construct $p(\Delta T_{>1})$, where $\Delta T_{>1}$ corresponds to the waiting time for subsequent kills. The distribution of $p(\Delta T_{>1})$ is identical to $p(\Delta t)$ from Fig. 2. One-sided Mann–Whitney *u* tests of $p(\Delta T_1)_{\mathrm{HeLa}}$ versus $p(\Delta T_{>1})_{\mathrm{HeLa}}$ and $p(\Delta T_1)_{\mathrm{MCF7}}$ versus $p(\Delta T_{>1})_{\mathrm{MCF7}}$ have *P* values of 0.017 and 1×10^{-10} respectively (Fig. S9 *E* and *F*), indicating that first kill times are statistically slower than waiting times. Furthermore, we find that $\langle p(\Delta T_1)\rangle$ is greater than $\langle p(\Delta T_{>1})\rangle$ for both HeLa and MCF7 targets, with $\langle p(\Delta T_1)\rangle_{\mathrm{HeLa}} - \langle p(\Delta T_{>1})\rangle_{\mathrm{HeLa}} = 22 \pm 9$ and $\langle p(\Delta T_1)\rangle_{\mathrm{MCF7}} - \langle p(\Delta T_{>1})\rangle_{\mathrm{MCF7}} = 62 \pm 10$. Thus, for both HeLa and MCF7, the first kill proceeds more slowly than subsequent kills, with the effect being more pronounced for MCF7 targets than for HeLa targets, both by magnitude and statistical likelihood of the conclusion.

From this analysis, we also conclude that first kills are slower than subsequent kills, consistent with the analysis in the main text.

Assessing Search-Time Model with HeLa Dilutions. At high HeLa densities, we expect a short search time for HeLa targets and a high number of effectors killing HeLa targets. At low HeLa densities, we expect a long search time for HeLa targets. We also expect a low number of effectors killing HeLa targets because there are not enough HeLa targets to kill. Thus, there should be an inverse relationship between the mean first HeLa kill time and the number of successful effectors with at least one HeLa kill. We measured the relationship between $\langle t_1\rangle$ and the number of successful effectors for the different HeLa densities (Fig. 3*D*). If MCF7 killing is due to a sparse fraction of MCF7 targets that have similar killing kinetics to HeLa targets, the data point for MCF7 should overlay the HeLa dilution curve. Instead, we observe that MCF7 is an outlier. Only highly diluted HeLa targets have a $\langle t_1\rangle$ similar to 100% MCF7 targets, but at that dilution, the number of successful effectors for HeLa is much lower than for MCF7. Conversely, a HeLa target dilution that has a similar number of successful effectors as 100% MCF7 targets has a much shorter $\langle t_1\rangle$. Thus, the data do not support the search-time model.

The interpretation of the experiment is valid because of self-consistency. For example, in the hypothetical case that an effector first kills an MCF7 target before a HeLa target, the measured first kill time for HeLa targets would be incorrect, because only HeLa targets are fluorescent and measured in the dilution experiments. However, MCF7 has a $\langle t_1\rangle$ that is much longer than any, except the very last, HeLa dilution, so it is unlikely, on average, that an MCF7 target is killed before a HeLa target. If most effector cells killed MCF7 targets before HeLa targets, the value of $\langle t_1\rangle$ for HeLa dilutions would be greater than the value for MCF7, but the dilution values are not greater. Another possibility is that MCF7 cells immobilize effector cells, but the motility data shows that effector cells are in fact more mobile on MCF7 targets. For these reasons, the data are self-consistent and supports the interpretation of Fig. 3*D*.

1. Mancini M, et al. (2000) Caspase-2 is localized at the Golgi complex and cleaves golgin-160 during apoptosis. *J Cell Biol* 149(3):603–612.
2. Nicolier M, Decrion-Barthod AZ, Launay S, Prétet JL, Mougin C (2009) Spatiotemporal activation of caspase-dependent and -independent pathways in staurosporine-induced apoptosis of p53wt and p53mt human cervical carcinoma cells. *Biol Cell* 101(8): 455–467.
3. Wesselborg S, Engels IH, Rossmann E, Los M, Schulze-Osthoff K (1999) Anticancer drugs induce caspase-8/FLICE activation and apoptosis in the absence of CD95 receptor/ligand interaction. *Blood* 93(9):3053–3063.
4. Inoue S, Browne G, Melino G, Cohen GM (2009) Ordering of caspases in cells undergoing apoptosis by the intrinsic pathway. *Cell Death Differ* 16(7):1053–1061.
5. Wang X, et al. (2006) Protective role of Cop in Rip2/caspase-1/caspase-4-mediated HeLa cell death. *Biochim Biophys Acta* 1762(8):742–754.
6. Thornberry NA, et al. (1997) A combinatorial approach defines specificities of members of the caspase family and granzyme B. Functional relationships established for key mediators of apoptosis. *J Biol Chem* 272(29):17907–17911.
7. Martinvalet D, Walch M, Jensen DK, Thiery J, Lieberman J (2009) Granzyme A: Cell death–inducing protease, proinflammatory agent, or both? *Blood* 114(18):3969–3970.

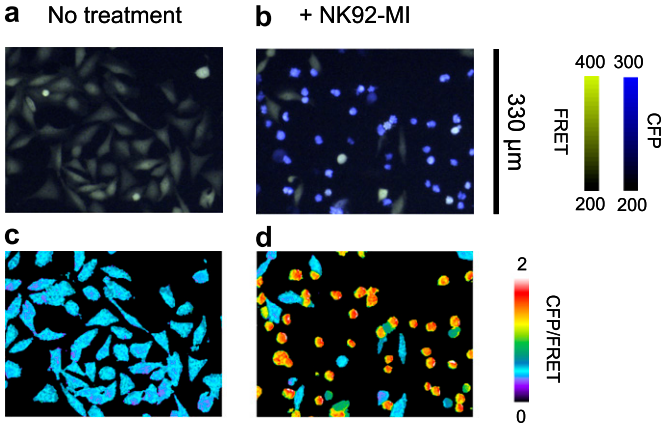

Fig. S1. Comparison of fluorescence image overlay and ratio. (*A* and *B*) Overlay of CFP (blue) and FRET (yellow) emissions for HeLa cells stably expressing the GzmB reporter in the absence (*A*) or presence (*B*) of NK92-MI effector cells. (*C* and *D*) Ratio of background subtracted CFP and FRET emissions for HeLa cells stably expressing the GzmB reporter in the absence (*C*) or presence (*D*) of NK92-MI effector cells. The image overlay accurately reflects the changes in the FRET reporter activity, as indicated by the correspondence between the two methods of presenting the data.

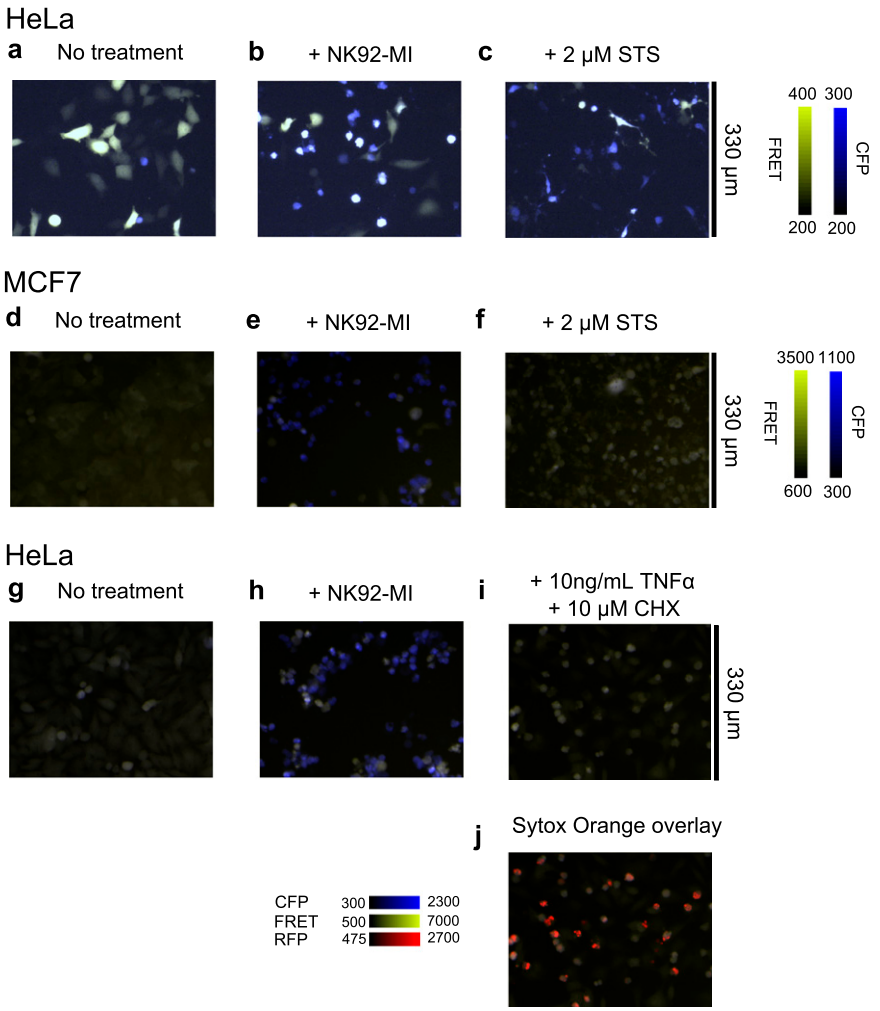

Fig. S2. Additional control data defining the GzmB reporter specificity. Staurosporine activates caspases in HeLa cells. (*A–C*) HeLa cells transfected with the caspase-3 FRET reporter EC-RP (1) after 4 h of no treatment (*A*), treatment with 1:1 NK92-MI cells (*B*), or treatment with staurosporine (*C*). The GzmB reporter shows no response in HeLa cells treated with staurosporine (Fig. 1*D*), indicating that apoptotic caspase activity does not cleave the GzmB reporter. (*D–F*) Staurosporine does not activate the GzmB reporter in MCF7 cells. MCF7 cells stably expressing the GzmB reporter after 6 h of no treatment (*D*), treatment with 3:1 NK92-MI cells (*E*), or treatment with staurosporine (*F*). The GzmB reporter shows no response to staurosporine in MCF7 cells. (*G–I*) TNFα treatment does not activate the GzmB reporter in HeLa cells. HeLa cells stably expressing the GzmB reporter after 6 h of no treatment (*G*), treatment with 3:1 NK92-MI cells (*H*), or treatment with TNFα and cycloheximide (CHX) at the indicated dose (*I*). An overlay of Sytox Orange (*J*) shows that the small rounded bodies formed after TNFα treatment are dead cells. However, the GzmB reporter was not activated during the treatment. *A–C* were obtained on the microscope described in *Materials and Methods*, whereas *D–J* were taken with a Nikon TE300 equipped with an ORCA-ER CCD camera mercury burner, and Metamorph software, which is why the absolute image scaling values are different.

1. Albeck JG, et al. (2008) Quantitative analysis of pathways controlling extrinsic apoptosis in single cells. *Mol Cell* 30(1):11–25.

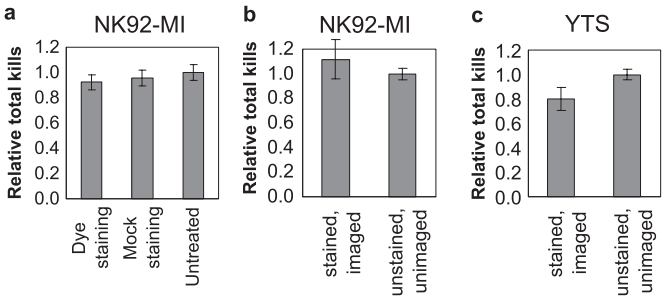

Fig. S3. (*A*) CellTracker Orange staining does not affect killing activity. NK92-MI cells were stained with CellTracker Orange as indicated in *Methods*, stained with mock DMSO, or untreated. After counting cells on a hemacytometer, equal numbers of NK92-MI cells were added to wells containing equal numbers of HeLa targets expressing the GzmB-reporter, and total kills were measured for the three samples. The bar graph shows the relative total killing, normalized by the untreated sample along with SEs. (*B*) Identical numbers of CellTracker Orange stained and unstained NK92-MI cells were added to wells of the same 96-well plate. The stained cells were imaged for 6 h under standard conditions, and unstained cells were not imaged. After 6 h, total kills were measured for the two conditions, to deterimine the combined effect of dye staining and phototoxicity on killing activity. *B* shows that there was no significant effect of staining and phototoxicity. (*C*) Identical numbers of CellTracker Orange stained and unstained YTS cells were added to wells of the same 96-well plate. The stained cells were imaged for 18 h, and unstained cells were not imaged. After 18 h, total kills were measured for the two conditions to deterimine the combined effect of dye staining and phototoxicity on killing activity. *C* shows that there was only a minor effect of staining and phototoxicity after 18 h.

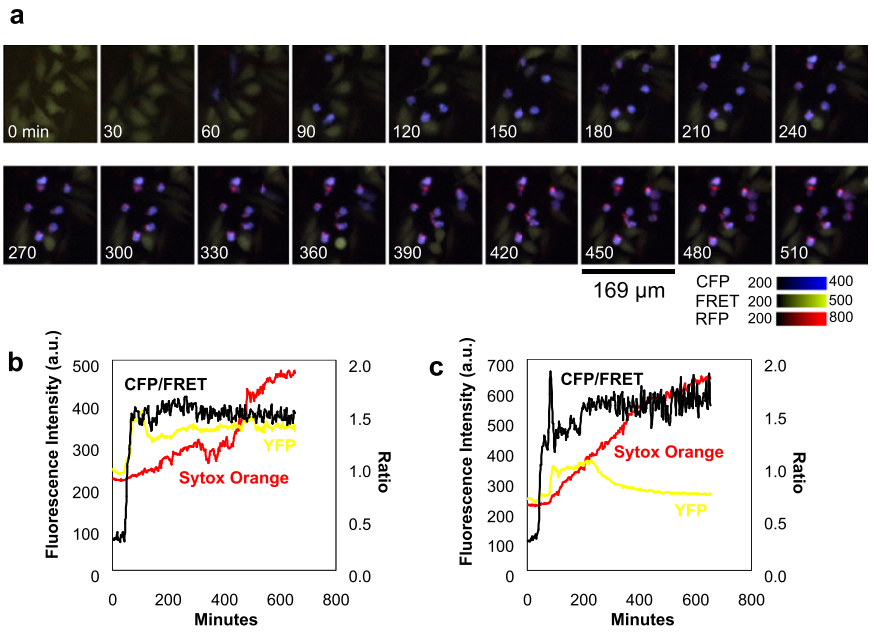

Fig. S4. Membrane permeability and lysis are slow following GzmB activity. (*A*) HeLa targets stably expressing the GzmB reporter are imaged during cytotoxic attack in the presence of 0.5 μM of the membrane impermeable DNA stain Sytox Orange (Invitrogen). Single-cell fluorescence traces over time are presented. An increase in red fluorescence indicates membrane permeabilization. All cells with a positive GzmB signal lead to membrane permeabilization, as determined by DNA staining. (*B*) Typical single-cell trace of reporters. The ratio of CFP to FRET emission (black, right axis) shows a sharp transition after cytotoxic attack. The membrane permeability, measured by the fluorescence intensity of Sytox Orange (red, left axis), shows a slow change until several hours after the GzmB signal, after which it increases rapidly. The intensity of the YFP signal (yellow, left axis) shows an abrupt increase, corresponding to cell rounding after cytotoxic attack, but no decrease over the course of many hours. These results are typical for the majority of target cells. The slow DNA dye kinetics and lack of YFP loss show that membrane permeabilization is slow. The delay between cytotoxic attack, as measured by morphology, and membrane permeabilization, as measured by a DNA dye, has been reported to be approximately 1.5 h (1). (*C*) For a small fraction of target cells (<5%), the membrane rapidly disintegrates after cytotoxic attack, leading to a rapid rise in Sytox Orange signal and a loss of YFP signal over time. For virtually every observed case, a positive GzmB signal always leads to cell death measured by membrane permeabilization, whether the permeabilization is slow or fast.

1. Waterhouse NJ, et al. (2006) Cytotoxic T lymphocyte-induced killing in the absence of granzymes A and B is unique and distinct from both apoptosis and perforin-dependent lysis. *J Cell Biol* 173(1):133–144.

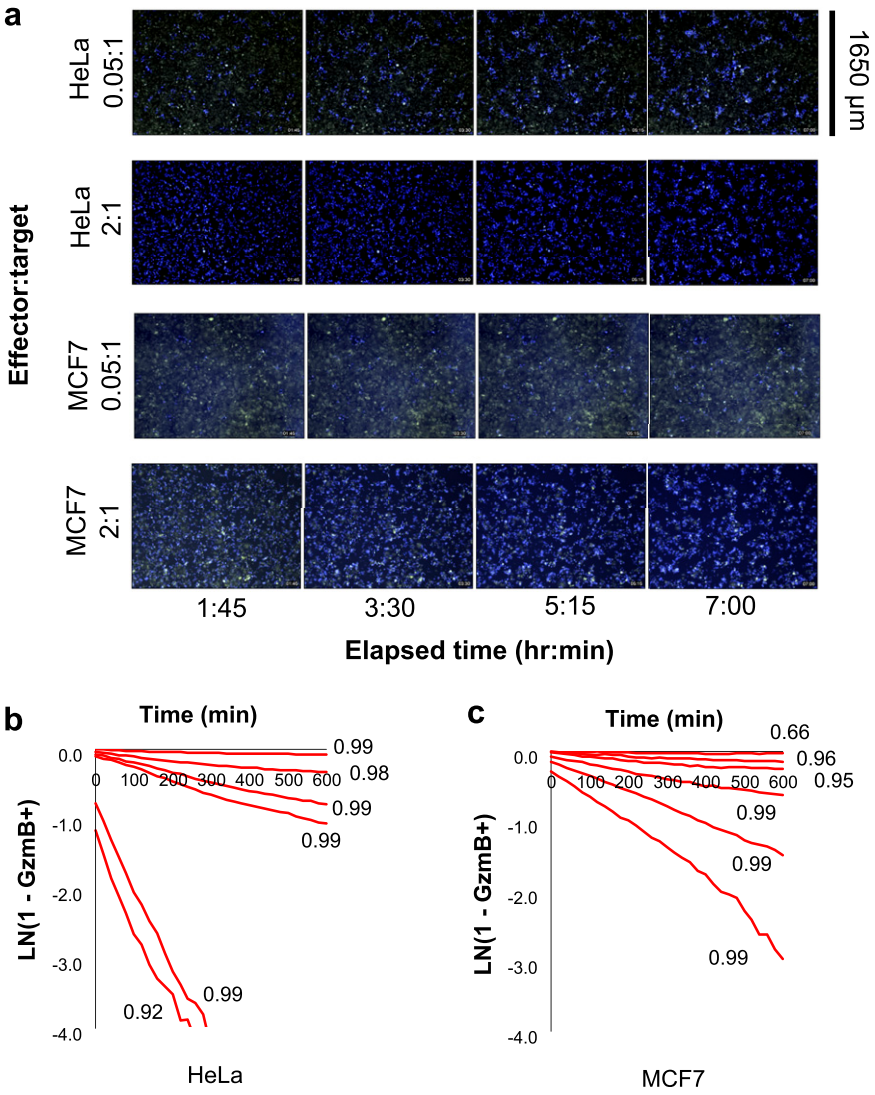

Fig. S5. Killing of HeLa and MCF7 targets by NK92-MI effectors at different effector:target ratios. (*A*) The 2×10^4 HeLa targets or 3×10^4 MCF7 targets stably expressing the GrzB reporter are incubated in a well of a 96-well plate with the number of NK92-MI cells giving the indicated ratios. A fluorescence overlay of the CFP (blue) and FRET (yellow) emissions shows white and blue targets for $GrzB^-$ and $GrzB^+$ targets, respectively, during a time course of killing. (*B* and *C*) Logarithmic survival plots of HeLa (*B*) and MCF7 (*C*) calculated from the bulk killing kinetics in Fig. 1 show linear decays, with the indicated r^2 values. The linear fits, consistent with a single, uniform killing rate, show that the bulk measurement does not reveal any heterogeneity target responses at high effector-to-target ratios. The deviation from linearity for the $r^2 = 0.66$ case is due to measurement noise in the bulk assay at very low levels of killing.

a

	HeLa			MCF7		
	λ	χ^2	p	λ	χ^2	p
$\lambda^k e^{-\lambda}/k!$	4.2	1200	$<10^{-4}$	2.9	600	0.0005
$\frac{\lambda^k e^{-\lambda}/k!}{1-e^{-\lambda}}$, $k>0$	5.8	66	$<10^{-4}$	3.7	83	0.0058
$(1-\lambda)^k\lambda$	0.16	45	$<10^{-4}$	0.31	18	0.20
$(1-\lambda)^{k-1}\lambda$, $k>0$	0.13	34	0.0016	0.29	16	0.25

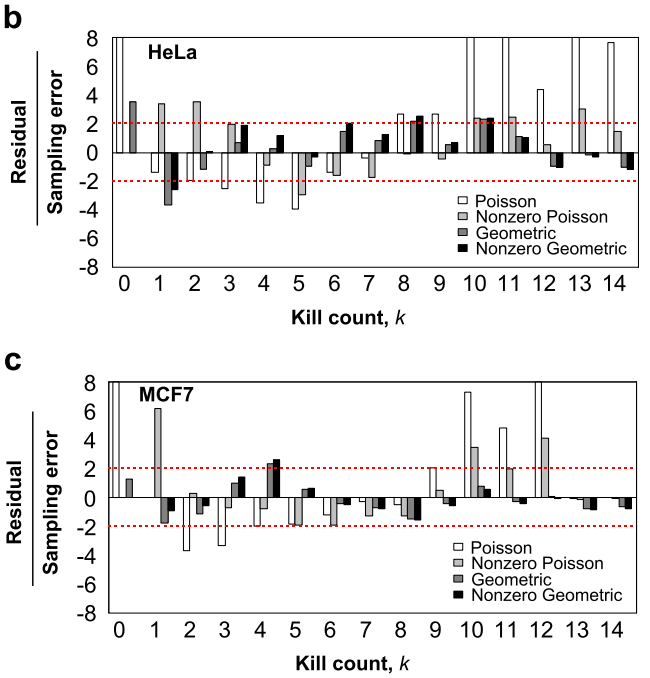

Fig. S6. Fitting of kill count distributions. (*A*) Best-fit parameters for the Poisson distribution, nonzero Poisson distribution, geometric distribution, and nonzero geometric distribution. For the nonzero distributions, the fit was applied to kill counts $k > 0$, and the distribution was renormalized as indicated in the first column. The fitting parameter, λ, the χ^2 value, χ^2, and the *P* value, *p*, are listed for the fits to kill counts on HeLa and MCF7 targets. *P* values were determined by randomly drawing from the best-fit distribution using an identical sample size as the observed measurement for 10^4 simulated datasets, calculating the corresponding set of $\{\chi^2_1 \ldots \chi^2_{10,000}\}$, and determining the rank of the observed χ^2. (*B* and *C*) The deviation of the observed distribution from the fitted distributions for HeLa (*B*) and MCF7 (*C*) targets is represented at each bin by a Z score, given as the residual divided by the sampling error. The sampling error is taken as the square root of the expected count at each bin. Both the HeLa and MCF7 kill counts have more observations at large *k* than expected for a Poisson process.

a

	HeLa			MCF7		
	(min) t_1,t_2	χ^2	p	(min) t_1,t_2	χ^2	p
$e^{-t/t_1}/t_1$	44	37	1.0	56	32	1.0
$\frac{e^{-t/t_1}-e^{-t/t_2}}{t_1-t_2}$	7.0, 42	46	0.018	5.0, 55	35	0.015

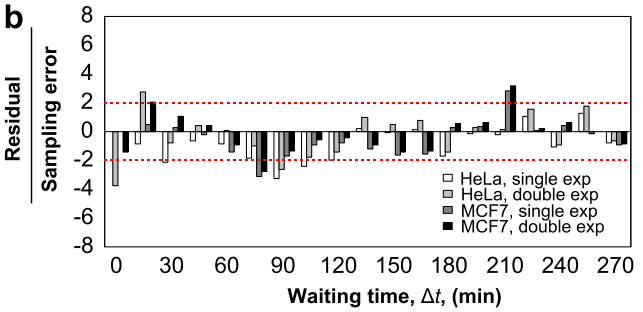

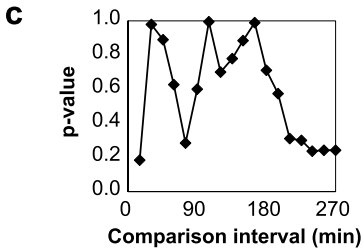

Fig. S7. Fitting and analysis of waiting time distributions. (*A*) Best-fit parameters for the exponential and double exponential waiting time distribution functions corresponding to one and two sequential rate-limiting steps, respectively. For the single exponential fit, the first bin was ignored. In practice, the fit was performed after shifting the other bins left by one place. The fitting parameters, t_1 and t_2, the χ^2 value, χ^2, and the *P* value, *p*, are listed for the fits to waiting times on HeLa and MCF7 targets. *P* values were determined by randomly drawing from the best-fit distribution using an identical sample size as the observed measurement for 10^4 simulated datasets, calculating the corresponding set of $\{\chi^2_1 \ldots \chi^2_{10,000}\}$, and determining the rank of the observed χ^2. (*B*) The deviation of the observed distribution from the fitted distributions for HeLa and MCF7 targets is represented at each bin by a Z score, given as the residual divided by the sampling error. The sampling error is taken as the square root of the expected count at each bin. Both the HeLa and MCF7 waiting times have more observations at long waiting times than expected by the fitted exponential distributions. (*C*) The Mann–Whitney *u* test was performed on the HeLa and MCF7 waiting time distributions. The two-sided *P* value is reported across various comparison intervals. For example, the 270-min interval includes the entire dataset. The 180-min interval includes waiting times from both distributions that were 180 min or less. The waiting times for HeLa and MCF7 are not significantly larger or smaller than each other, and differences are most likely the result of events with very long waiting times.

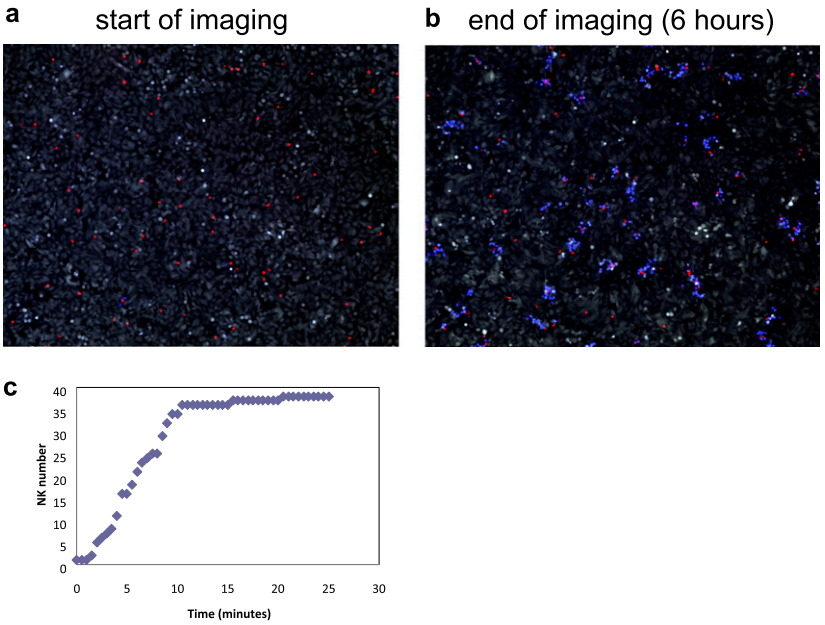

Fig. S8. Effect of settling time on imaging experiment. (*A*) Full field of view of first imaging frame in a typical timelapse. (*B*) Full field of view after 6 h of imaging. The number of NK cells is relatively unchanged, indicating that settling of NK cells during the course of the experiment was negligible. (*C*) Measurement of settling time. Fifty microliters of stained NK cells in RPMI media were added to target cells in a well of a 96-well plate containing 50 μL of RPMI media. The microscope was previously focused on the layer of target cells, and after adding NK cells to a single well, imaging was begun immediately (in less than 30 s) with an acquisition rate of 1 frame every 30 s. The number of NK cells in the focal plane was counted over time, with almost all NK cells settling within 10 min. In a typical experiment, 40 wells are loaded with NK cells, and each XY position of the motorized stage is recorded afterward for the automated timelapse, along with setting of each Z position for the focal plane. This procedure typically takes more than 10 min, which is why all NK cells are settled by the first time-lapse image, as in *A*.

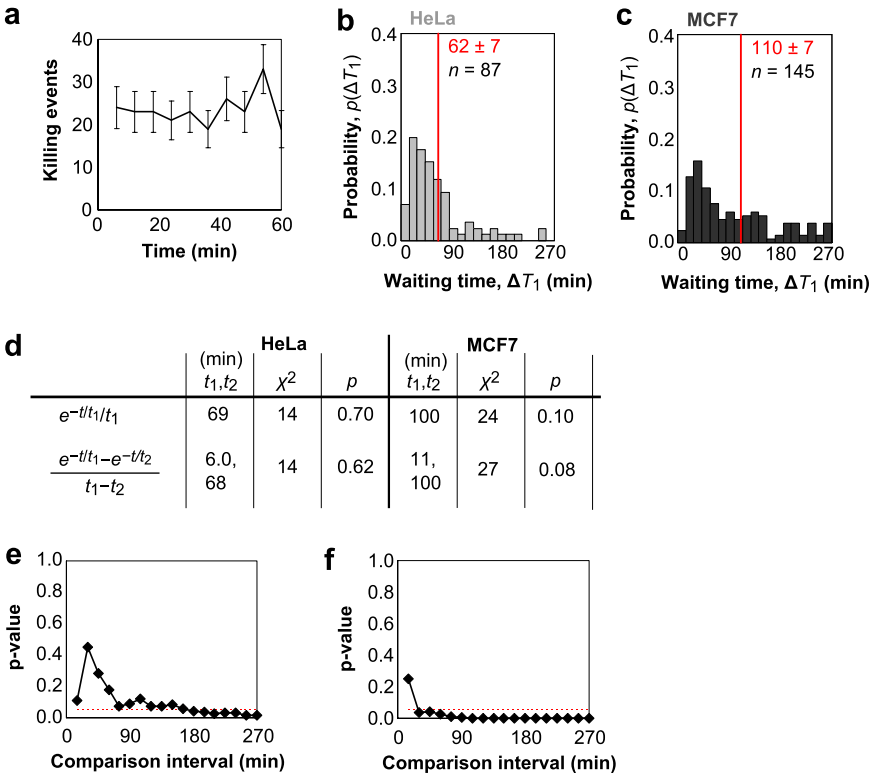

d

	HeLa (min) t_1,t_2	HeLa χ^2	HeLa p	MCF7 (min) t_1,t_2	MCF7 χ^2	MCF7 p
$e^{-t/t_1}/t_1$	69	14	0.70	100	24	0.10
$\frac{e^{-t/t_1}-e^{-t/t_2}}{t_1-t_2}$	6.0, 68	14	0.62	11, 100	27	0.08

Fig. S9. Analysis of waiting time distributions. (*A*) The total number of killing events per 6-min window is plotted for HeLa targets from the start of imaging at $t = 0$. Error bars denote square-root-n counting error. The flat line indicates that there is no substantial change in killing during the first hour of imaging. (*B* and *C*) First kill time distributions for HeLa (*B*) and MCF7 (*C*) targets, only for first kills occurring on or after $t = 3$ min, as described in the *SI Results and Discussion*. The reference $t = 3$ min is used as a zero point, so the histograms are not identical to Fig. 2 *F* and *G*. (*D*) Best-fit parameters for first kill times. The fitting procedure is the same as in Fig. S7*A*. (*E* and *F*) The Mann–Whitney *u* test was performed on first kill times versus subsequent waiting times for HeLa (*E*) and MCF7 (*F*) targets by using the distributions in *B* and *C* and Fig. 2 *D* and *E*, as described in the *SI Results and Discussion*. The one-sided *P* value is reported across various comparison intervals. For example, the 270-min interval includes the entire data set. The 180-min interval includes waiting times from both distributions that were 180 min or less. The dashed red line indicates the level of $P = 0.05$.

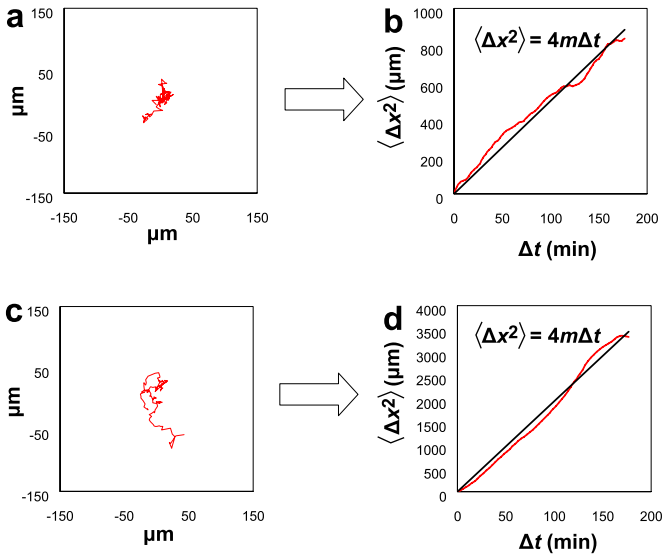

Fig. S10. Single-cell tracking and determination of motility coefficients. (*A*) Sample trace of NK92-MI effector moving on HeLa targets. (*B*) Sample curve for mean-squared displacement, $\langle \Delta x^2 \rangle$, versus elapsed time, Δt, of an individual effector cells on a HeLa target (red) by using internal averaging of displacement intervals. The two-dimensional motility coefficient, m, is calculated by fitting $\langle \Delta x^2 \rangle = 4m\Delta t$ (black), for individual cells to determine the values in Fig. 3*E*. (*C*) Sample trace of effector on MCF7 targets. (*D*) Sample curve for mean-square displacement versus elapsed time on MCF7 targets.

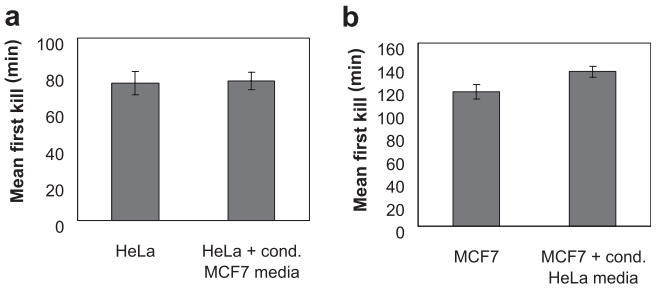

Fig. S11. Conditioned media does not alter the first killing time. HeLa cells were plated at 2×10^4 cells per 96 well in DMEM media overnight, and MCF7 were plated at 3×10^4 cells per 96 well in RPMI (Cellgro 10-040) media overnight. Before the experiment, media was removed from each well with a pipette and saved. Fifty microliters of RPMI was added to control samples. Fifty microliters of the recovered conditioned media was added to the appropriate test samples. NK92-MI cells were spun down and diluted in fresh RPMI media. Fifty microliters of the NK92-MI cells were added to each sample to give a final count of 500 effectors per well. (*A*) HeLa targets with and without MCF7 conditioned media showed similar first kill times. Error bars are SEs, and a total of 86 and 106 first kill times were recorded for the control and test samples, respectively. (*B*) MCF7 targets with and without HeLa conditioned media also showed similar first kill times. Error bars are SEs, and a total of 72 and 66 first kill times were recorded for the control and test samples, respectively. First kill times for HeLa targets were not slowed by the addition of 50% conditioned MCF7 media, and first kill times for MCF7 targets were not accelerated by the addition of 50% conditioned HeLa media.

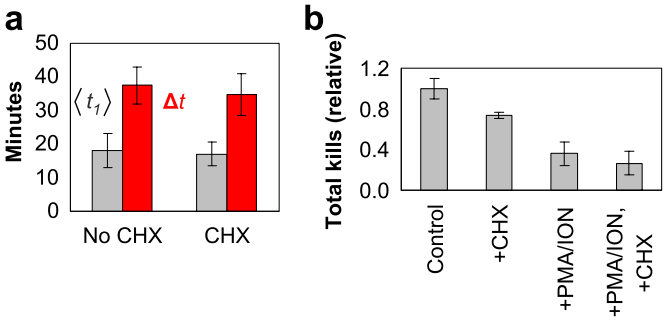

Fig. S12. Gene expression minimally affects short-term killing kinetics. (*A*) Average first kill (gray) times and waiting times (red) for NK92-MI effectors and HeLa targets in the absence (*Left*) and presence (*Right*) of 10 μg/mL cycloheximide. The kinetic parameters do not show a significant change over a 6-h imaging experiment. (*B*) Total killing activity, normalized by the untreated control, for NK92-MI effectors and HeLa targets. Effectors were untreated, treated with 10 μg/mL cyclohexidmide during the course of a 6-h imaging experiment, pretreated for 1 h with 1 μg/mL ionomycin and 30 ng/mL PMA before the killing assay, or subject to both treatments. Total killing was strongly inhibited only for effectors depleted by ionomycin/PMA treatment to force degranulation. The addition of cycloheximide to ionomycin/PMA treated effectors further reduces killing. Cycloheximide alone reduces total killing by only ~30%, indicating that the majority of the killing events during 6 h does not require de novo gene expression. The unchanged kinetics in the presence of cycloheximide implies that cells with insufficient protein expression stop participating in killing, whereas productive killing events occur with the same kinetics. The changes observed in total killing prove that the cycloheximide dose is effective in *A*. Hence, the observed bursting kinetics are not the result of de novo gene expression.

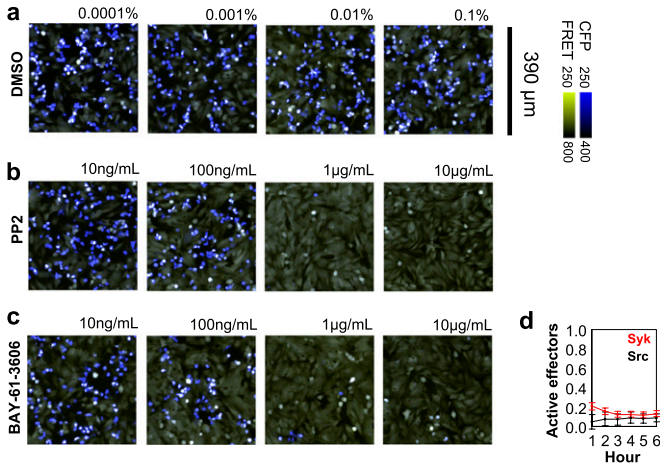

Fig. S13. Inhibition of NK killing by Src and Syk inhibition. (*A*–*C*) Overlay of CFP (blue) and FRET (yellow) emissions for HeLa cells stably expressing the GzmB reporter incubated for 6 h with NK92-MI effectors and the indicated concentration of the matching DMSO vehicle control (*A*), the Src inhibitor PP2 (*B*), or the Syk inhibitor BAY-61-3606 (*C*). (*D*) Microscopy was performed under standard conditions in the presence of 700 ng/mL PP2 or 500 ng/mL BAY-61-3606. The fraction of active effectors was plotted for each hour and shows a relatively constant level for both inhibitors. The same dataset is used in Fig. 3*G*, where overall killing is substantially reduced for both cases.

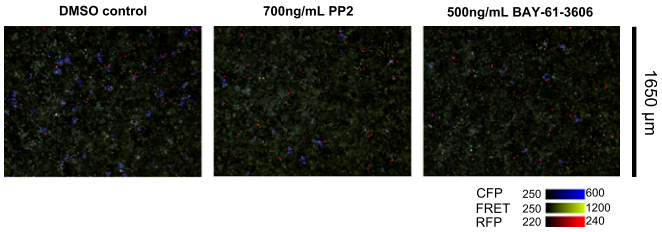

Fig. S14. Serial killing under partial Src or Syk inhibition. NK92-MI cells (red) serially kill HeLa targets expressing the GzmB reporter in the presence of 700 ng/mL of the Src inhibitor PP2 or 500 ng/mL Syk inhibitor BAY-61-3606. However, a smaller fraction of effector cells are active under drug treatment. A fluorescence overlay of the CFP (blue) and FRET (yellow) emissions shows white and blue targets for $GzmB^-$ and $GzmB^+$ targets, respectively, after 6-h incubation. Although killing is reduced, there are clusters of killed targets because of serial killing, rather than sparse single kills evenly spread throughout the field.

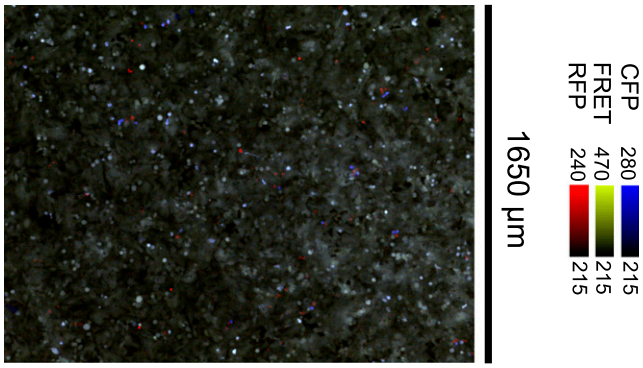

Fig. S15. Serial killing by YTS effector cells. The 2×10^4 HeLa targets stably expressing the GzmB reporter are incubated in a well of a 96-well plate with 1,000 YTS cells. A fluorescence overlay of the CFP (blue) and FRET (yellow) emissions shows white and blue targets for $GzmB^-$ and $GzmB^+$ targets, respectively. Effector cells stained with CellTracker Orange are imaged with RFP filters, overlaid in red. The image shows killing results after 18 h. Only a fraction of YTS cells has at least one kill during the elapsed time, but YTS cells engaging in killing display serial killing, indicated by clusters of blue target cells. The YTS cell stain is weaker after 18 h because of both loss of dye and dilution by cell division for some of the YTS cells. However, single YTS cells can still be clearly tracked in movies (Movie S7).

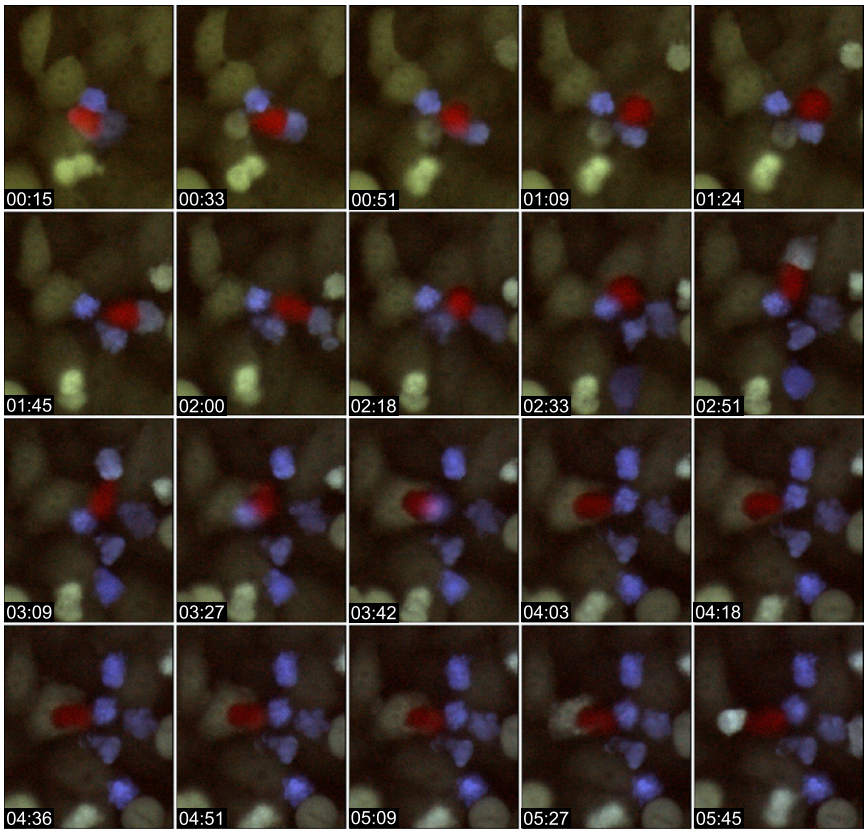

Fig. S16. Higher resolution time-lapse of serial killing by an NK92-MI effector cell. The 2×10^4 HeLa targets stably expressing the GzmB reporter are incubated in a well of a 96-well plate with 1,000 NK92-MI cells. A fluorescence overlay of the CFP (blue) and FRET (yellow) emissions shows white and blue targets for $GzmB^-$ and $GzmB^+$ targets, respectively. Effector cells stained with CellTracker Orange are imaged with RFP filters, overlaid in red. Imaging was performed as described in *Materials and Methods*, except a 20×/0.45 N.A. objective was used with no pixel binning. The time lapse for a single NK cell is shown.

Movie S1. GzmB activity is an early signal for cytotoxic attack. The calcium indicator R-GECO1 is constructed in the lentiviral backbone from pHR'CMVGFP_hRIF1(406-2446)IREShygro. Infection of HeLa targets stably expressing the GzmB reporter and flow sorting of positive clones generates a cell line with simultaneous calcium and GzmB reporters. The 2×10^4 HeLa targets stably expressing the GzmB reporter and the R-GECO1 calcium reporter are incubated in a well of a 96-well plate with 500 NK92-MI cells. A fluorescence overlay of the CFP (blue) and FRET (yellow) emissions shows white and blue targets for $GzmB^-$ and $GzmB^+$ targets, respectively. A fluorescence overlay of the RFP (red) emission shows the earliest calcium transient preceding GzmB activation by less than 30 min, and the strongest transient occurring immediately before GzmB activation. Calcium transients result from perforin damage of the membrane (1). Thus, GzmB activation quickly follows a cytotoxic attack in comparison with complete membrane permeabilization, as measured in Fig. S4. The timestamp displays the elapsed time in the format hours:minutes.

1. Thiery J, et al. (2011) Perforin pores in the endosomal membrane trigger the release of endocytosed granzyme B into the cytosol of target cells. *Nat Immunol* 12(8):770–777.

Movie S1

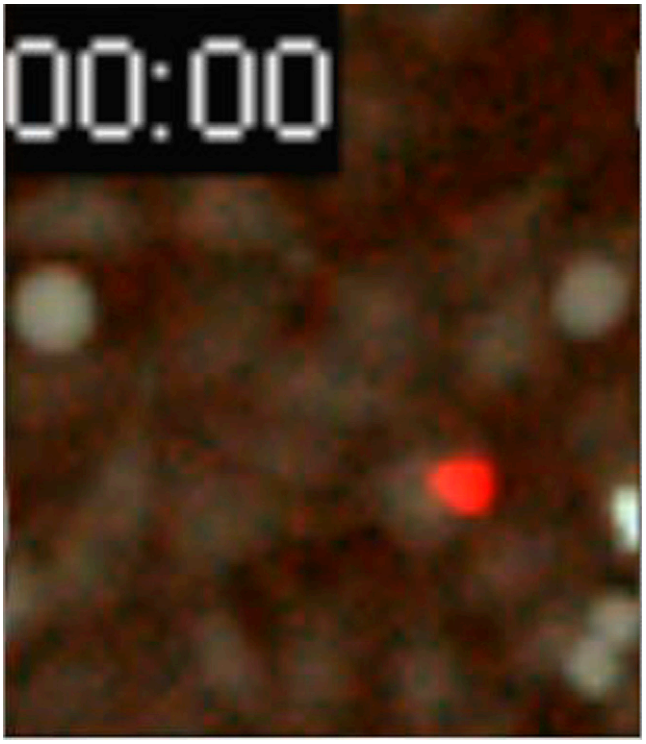

Movie S2. Serial killing of HeLa targets by single NK92-MI effector cells. The 2×10^4 HeLa targets stably expressing the GzmB reporter are incubated in a well of a 96-well plate with 500 NK92-MI cells. A fluorescence overlay of the CFP (blue) and FRET (yellow) emissions shows white and blue targets for $GzmB^-$ and $GzmB^+$ targets, respectively. Effector cells stained with CellTracker Orange are imaged with RFP filters, overlaid in red. Individual effector cells sequentially kill multiple targets. The timestamp displays the elapsed time in the format hours:minutes.

Movie S2

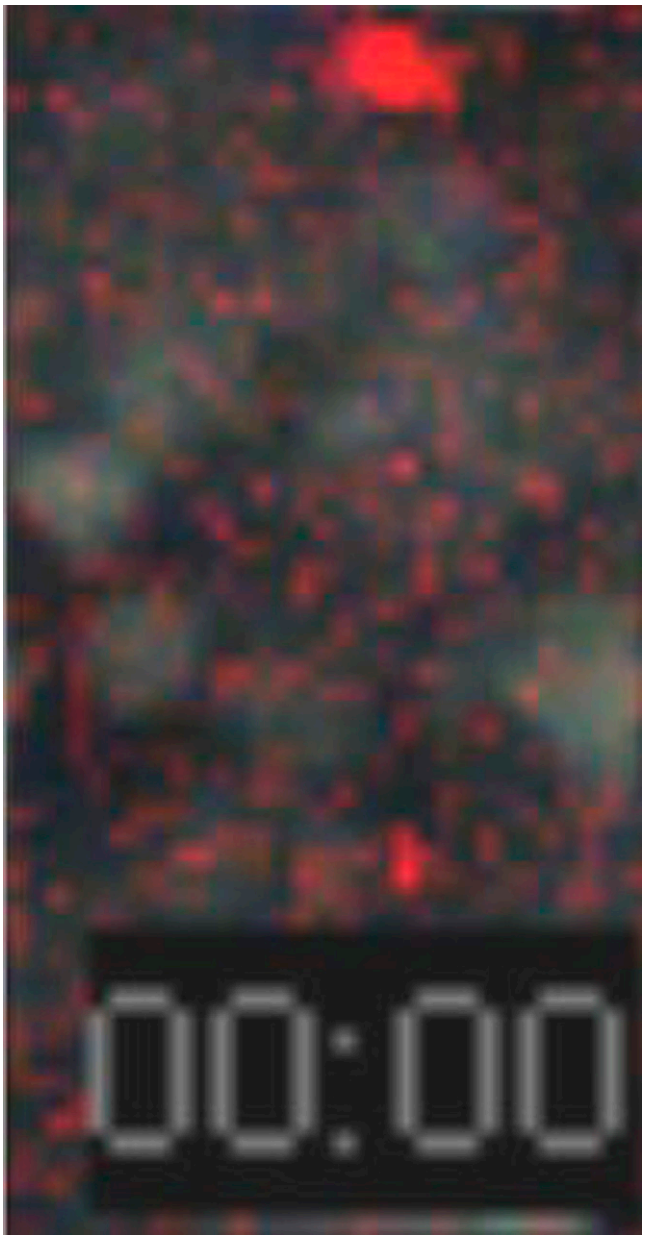

Movie S3. Serial killing of MCF7 targets by single NK92-MI effector cells. The 3×10^4 MCF7 targets stably expressing the GzmB reporter are incubated in a well of a 96-well plate with 500 NK92-MI cells. A fluorescence overlay of the CFP (blue) and FRET (yellow) emissions shows white and blue targets for $GzmB^-$ and $GzmB^+$ targets, respectively. Effector cells stained with CellTracker Orange are imaged with RFP filters, overlaid in red. Individual effector cells sequentially kill multiple targets. The timestamp displays the elapsed time in the format hours:minutes.

Movie S3

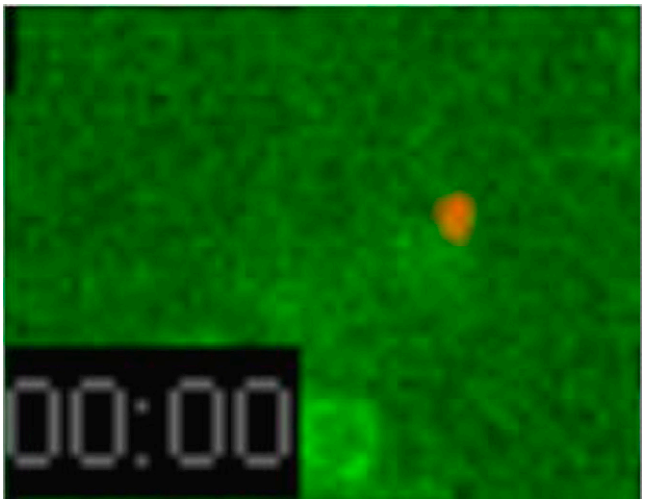

Movie S4. Serial cytotoxic attacks are sequential. The calcium indicator GCaMP3 is constructed in the lentiviral backbone from pLenti-CMV-GFP. Infection of HeLa targets and selection by G418 resulted in cells stably expressing the green calcium reporter. Sorting of positive clones generates a cell line with simultaneous calcium and GzmB reporters. The 2×10^4 HeLa targets stably expressing the GCaMP3 reporter are incubated in a well of a 96-well plate with 500 NK92-MI cells stained with CellTracker Orange. By visualizing the calcium transients with a 30-s frame rate, it is possible to see that serial killing consists of sequential events. The timestamp displays the elapsed time in the format hours:minutes.

Movie S4

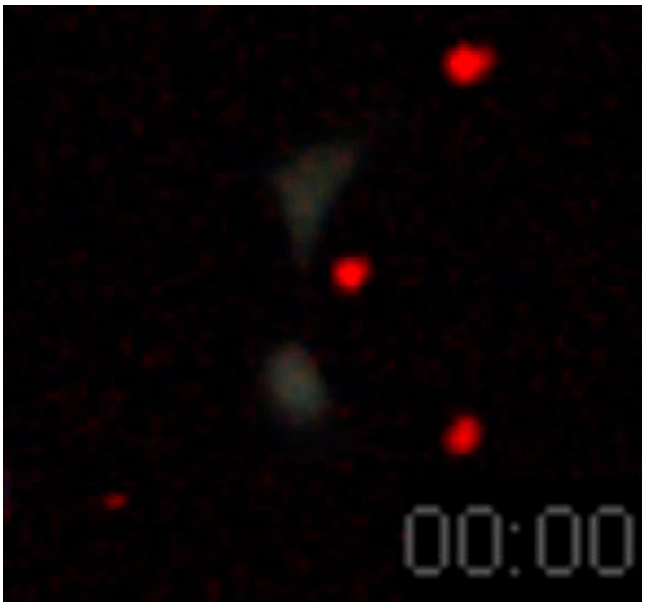

Movie S5. Persistence interaction with old targets. NK92-MI cells (red) stay attached to isolated targets long after delivering GzmB in the absence of other nearby targets. Each well of a 96-well plate contains 700 HeLa targets stably expressing the GzmB reporter. A fluorescence overlay of the CFP (blue) and FRET (yellow) emissions shows white and blue targets for $GzmB^-$ and $GzmB^+$ targets, respectively. The timestamp displays the elapsed time in the format hours:minutes.

Movie S5

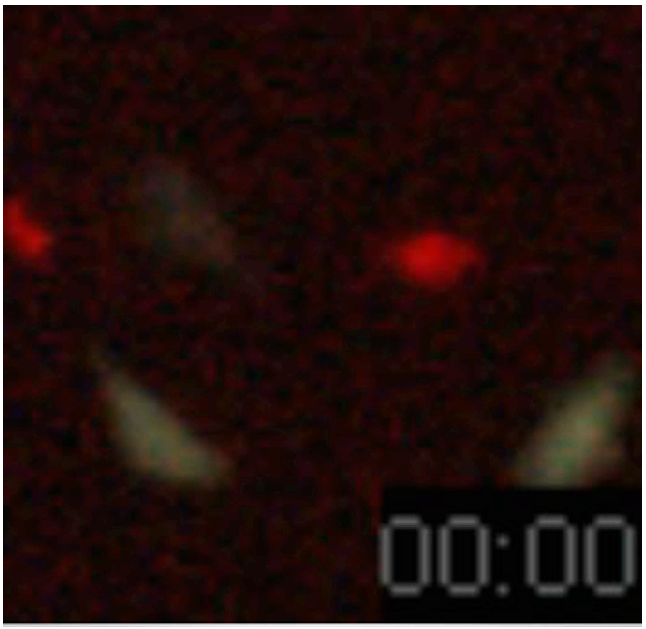

Movie S6. Detachment from old target in the presence of new targets. NK92-MI cells (red) detach from old targets in the presence of other nearby targets. Each well of a 96-well plate contains 700 HeLa targets stably expressing the GzmB reporter and an additional 2×10^4 nonfluorescent HeLa targets. A fluorescence overlay of the CFP (blue) and FRET (yellow) emissions shows white and blue targets for $GzmB^-$ and $GzmB^+$ targets, respectively. Nonfluorescent HeLa targets may be killed during the time lapse, but such killing would not be apparent in this movie. The timestamp displays the elapsed time in the format hours:minutes.

Movie S6

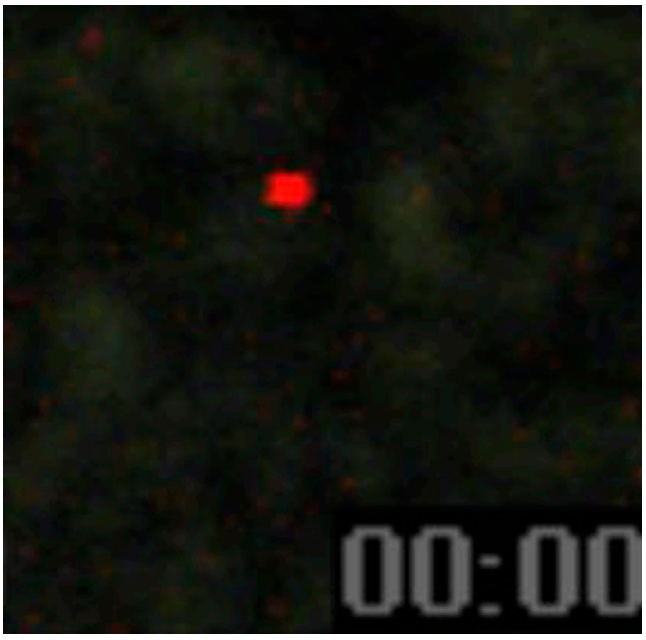

Movie S7. Serial killing of HeLa targets by single YTS effector cells. The 2×10^4 HeLa targets stably expressing the GzmB reporter are incubated in a well of a 96-well plate with 1,000 YTS cells. A fluorescence overlay of the CFP (blue) and FRET (yellow) emissions shows white and blue targets for $GzmB^-$ and $GzmB^+$ targets, respectively. Effector cells stained with CellTracker Orange are imaged with RFP filters, overlaid in red. Individual effector cells sequentially kill multiple targets. The timestamp displays the elapsed time in the format hours:minutes.

Movie S7